

Cite this: DOI: 10.1039/c8lc00593a

An optofluidic system with integrated microlens arrays for parallel imaging flow cytometry†

Gregor Holzner,^{‡,a} Ying Du,^{‡,ab} Xiaobao Cao,^a Jaebum Choo,^c Andrew J. deMello ^{ID, *a} and Stavros Stavrakis^{*a}

In recent years, high-speed imaging has become increasingly effective for the rapid analysis of single cells in flowing environments. Single cell imaging methods typically incorporate a minimum magnification of 10× when extracting sizing and morphological information. Although information content may be significantly enhanced by increasing magnification, this is accompanied by a corresponding reduction in field of view, and thus a decrease in the number of cells assayed per unit time. Accordingly, the acquisition of high resolution data from wide field views remains an unsolved challenge. To address this issue, we present an optofluidic flow cytometer integrating a refractive, microlens array (MLA) for imaging cells at high linear velocities, whilst maximizing the number of cells per field of view. To achieve this, we adopt an elasto-inertial approach for cell focusing within an array of parallel microfluidic channels, each equipped with a microlens. We characterize the optical performance of the microlenses in terms of image formation, magnification and resolution using both ray-tracing simulations and experimental measurements. Results demonstrate that the optofluidic platform can efficiently count and magnify micron-sized objects up to 4 times. Finally, we demonstrate the capabilities of the platform as an imaging flow cyclometer, demonstrating the efficient discrimination of hB and Jurkat cells at throughputs up to 50 000 cells per second.

Received 11th June 2018,
Accepted 15th October 2018

DOI: 10.1039/c8lc00593a

rsc.li/loc

1. Introduction

Optical imaging methods have conventionally been used for detecting and visualizing small numbers of micron-sized, quasi-static objects such as cells and microparticles. They provide for high resolution cellular imaging (enabled by the efficient light collecting capabilities of modern objective lenses) and in turn the extraction of precise information regarding cellular size, shape, structure and morphology.¹ However, by definition, high numerical aperture (NA), high magnification lenses have reduced fields of view (FOV) (typically between 100 and 500 μm), which limits their utility in imaging extended regions of space; a desirable capability in techniques such as imaging flow cytometry (FC). Recently it was demonstrated that both spherical or hemispherical microlenses lenses with diameters of approximately 60 μm can mimic the

optical performance of conventional low magnification objective lenses.^{2,3} In this respect, such microlenses have been successfully used to increase light coupling efficiencies into and out of waveguides,^{4,5} enhance fluorescence signals associated with moving cells⁶ and image fluorescent microparticles³ and blood cells.⁷ That said, hemispherical microlenses are better suited to the imaging of micron-sized objects, since spherical aberrations are significantly reduced.⁶ Moreover, hemispherical microlenses can be manufactured *via* a range of different methods including femtosecond laser polymerization,⁴ ink jet processing of UV curable polymers,⁸ hot embossing,⁹ micro-molding^{10,11} and photoresist reflow techniques.¹² Of these, the most common and developed method for hemispherical microlens fabrication is the reflow technique, which is both facile and low-cost in creating components for image sensing,¹³ fluorescence detection¹⁴ and high-resolution fluorescence scanning microscopy.^{15,16} Interestingly, very few studies have investigated the integration of microlenses within microfluidic devices for imaging flowing objects. This is primarily due to the fact that most microlens arrays are best suited for simultaneous imaging of static, micron-sized objects spread over large areas. That said, a small number of studies have reported the integration of diffractive lens arrays integrated within microfluidic platforms for fluorescence detection of rapidly moving microdroplets¹⁵ and bright field imaging of flowing cells.¹⁶ However, the limited focal ranges and

^a Institute for Chemical and Bioengineering, Department of Chemistry and Applied Biosciences, ETH Zürich, Vladimir Prelog Weg 1, 8093 Zürich, Switzerland.

E-mail: andrew.demello@chem.ethz.ch, stavros.stavrakis@chem.ethz.ch;

Tel: +41 44 633 66 10

^b College of Sciences, Zhejiang University of Technology, Hangzhou 310023, China

^c Department of Bionano Technology, Hanyang University, Ansan 15588, South Korea

† Electronic supplementary information (ESI) available: Supplementary Fig. S1–S6 and Table S1. See DOI: 10.1039/c8lc00593a

‡ G. H. and Y. D. contributed equally to this work.

chromatic aberration of these diffractive lenses have limited their application to bright field imaging of cells and particles with diameters less than 6 μm and at throughputs of ~ 2000 cells per s.¹⁶

In recent years, chip-based microfluidic systems have emerged as attractive formats in which to perform flow cytometry.¹⁷ Put simply, microfluidic platforms offer several advantages over traditional macroscale formats, including reduced sample and sheath flow requirements, low unit costs and ease of operation. Unsurprisingly, much recent research activity has focused on the development of microfluidic cell manipulation techniques that enable efficient focusing of cells into single file flows. For example, a number of studies have shown that particles and cells flowing through microchannels can be made to migrate and focus at certain positions across the channel cross-section under the influence of inertial¹⁸ or elasto-inertial forces.^{19,20} However, several technical barriers, associated with parallel cell sample focusing, high sensitivity detection and device fabrication have limited applications of microfluidic flow cytometers in ultra high throughput detection.

A direct way of increasing the throughput of a microfluidic system is through parallelization. However, the realization of high-resolution imaging within parallel microfluidic formats using low NA objectives (needed for large field of view experiments) is an immense challenge. One route for improving imaging throughput is the implementation of an array of compound microlenses embedded in the microfluidic device. Herein, we present an optofluidic platform that integrates refractive arrays of hemispherical microlenses with parallel microfluidic channels. Moreover, we utilize an elasto-inertial flow focusing method^{19–21} to precisely focus mammalian cells (having diameters between 8 and 10 μm) in one plane at the center of the channel. We subsequently use both optical simulations and experiments to assess the impact of lens diameter (d) and height (h) on focal length, numerical aperture (NA) and image formation. Finally, the optimized optofluidic system is used to simultaneously count and image cellular populations at a throughput of up to 50 000 cells per second.

2. Materials and methods

2.1 Cell culture

Cell-based experiments were performed with Jurkat (Sigma-Aldrich, Buchs, Switzerland) and human B lymphocytes cell lines. Cell lines were initially tested for mycoplasma contamination and then cultured in RPMI-1640 medium (Life Technologies, Zug, Switzerland) supplemented with 10% (v/v) FBS (Life Technologies, Zug, Switzerland) and 1% (v/v) penicillin-streptomycin (10 000 U mL⁻¹, Life Technologies, Zug, Switzerland) in a New Brunswick Galaxy170S CO₂ incubator (Eppendorf, Basel, Switzerland) at 37 °C and 5% CO₂. Cells were split every two days to maintain a concentration of approximately 2×10^5 viable cells per ml. All the experiments were performed on cells in the exponential (log) phase of growth.

2.2 Lens and microfluidic device fabrication

Microfabrication of the optofluidic platform consists of four steps. In the first, a SU-8 master structure (of the microfluidic channel pattern) is fabricated using standard photolithography. Second, the PDMS microfluidic device is cast from the SU-8 master mold. Third, the microlens array is formed on 50 μm thick cover glass (D263, Schott Glass, Mainz, Germany) using a thermal reflow process. In the last step, the PDMS and the cover slip are covalently bonded together under an oxygen plasma.

Briefly, the two-dimensional channel pattern was designed using AutoCAD 2014 (Autodesk, San Rafael, USA) and printed onto a transparent film photomask (Micro Lithography Services Ltd, Chelmsford, United Kingdom). This photomask was then used to pattern an SU-8 (Microchem Corporation, Westborough, USA) film on a silicon wafer *via* conventional photolithography. Subsequently, a 10:1 mixture of PDMS monomer and curing agent (Sylgard 184, Dow Corning, Midland, USA) was poured over the master-mold, polymerized at 70 °C for 4 hours and then peeled off. Inlet and outlet ports were punched using a hole-puncher (Technical Innovations, West Palm Beach, USA) and the structured PDMS substrate then bonded to the glass substrate containing the microlens array, after treating both surfaces in an air plasma (EMITECH K1000X, Quorum Technologies, East Sussex, United Kingdom) for 60 seconds. Alignment of the PDMS channel with the microlens array was performed using a home-made alignment tool (an xyz-stage combined with a camera). All channels were designed to be 53 μm high and 53 μm wide, to achieve a blockage ratio $\beta < 0.24$ for efficient single file focusing.¹⁹ The blockage ratio is the quotient of the cell diameter and the channel dimension.

Microlenses were fabricated on a planar 50 μm thick glass substrate *via* a reflow molding process, in which surface tension drives a photoresist to form a smooth and curved spherical surface.^{22,23} After depositing a layer of AZ40XT photoresist (MicroChemicals GmbH, Ulm, Germany) of the desired thickness onto a glass coverslip (Schott Ag, Mainz, Germany), cylindrical posts were defined using standard photolithography. The glass coverslip supporting the microstructures was then placed onto a hotplate and heated to a temperature at 142 °C for 75 seconds. To allow the forming microlenses to harden in a uniform manner, the hotplate temperature was switched off to cool the sample gradually to room temperature over a period of three hours. Finally, an ULTRA 55 scanning electron microscope (Zeiss, Oberkochen, Germany) was used to image and characterize the cross sectional profile of individual lenses.

2.3 Device operation

The complete microfluidic device was placed onto a motorized x-y translation stage (Mad City Laboratories, Madison, USA) mounted on an inverted microscope (Nikon Ti-E Microscope, Zurich, Switzerland). A cell suspension (~ 5 million cells per ml) was then loaded into a 1 ml gastight syringe

(Hamilton Laboratory Products, Nevada, USA) and delivered into the microfluidic device at a flow rate of $90 \mu\text{L min}^{-1}$ using a precision syringe pump Pico Plus Elite (Harvard Apparatus, Holliston, USA). The cell suspension consists of DPBS buffer, 36% (v/v) OptiPrepTM and 500 or 1000 ppm of an aged 0.4 MDa polyethylene oxide (PEO, Sigma-Aldrich, Buchs, Switzerland) viscoelastic solution.¹⁹ The master PEO solution was prepared by thoroughly dissolving PEO of low molecular weight (0.4 MDa and 1 MDa) in phosphate buffered solution (DPBS, Life Technologies, Zug, Switzerland) to a concentration of 10 g L^{-1} . Solutions were allowed to age at room temperature for one month prior to use. Master solutions were then diluted to the desired concentration prior to experiment. Settling of the cell suspension in the syringe was prevented by matching the density of the medium to the cell suspension with OptiprepTM density gradient medium (Sigma-Aldrich, Buchs, Switzerland). Microfluidic channels were treated with Pluronic F127 (Sigma Aldrich, Buchs, Switzerland) prior to the experiment to prevent cell adhesion to channel surfaces. Images were obtained using an Eclipse Ti-E inverted microscope (Nikon, Zurich, Switzerland) equipped with Nikon objectives: Plan Apo $2\times 0.10 \text{ NA}$ and Plan Apo $4\times 0.20 \text{ NA}$. A high speed camera (IDT Motion Pro Y5.1, Niederoenz, Switzerland) was used to record images during flow cytometry experiments. Images of beads and cells were analyzed using ImageJ,²⁴ in house Python scripts and the computer vision library OpenCV (opencv.org). The different image processing stages are shown and explained in Fig. S-1 and Note S-1.[†]

3. Results and discussion

3.1 Cell focusing device

A schematic of the microfluidic device consisting of a series of parallel channels is shown in Fig. 1a. The cross-sectional dimensions of these channels ($53 \mu\text{m width} \times 53 \mu\text{m height}$) are designed to effectively focus cells (using elasto-inertial forces) to a single file at the center of the channel by maintaining a blockage ratio below 0.25.¹⁹ Moreover, the concentration and molecular weight of the carrier PEO solution was adjusted to focus beads (1 MDa) and cells (0.4 MDa) at flow rates suitable for high throughput imaging.^{19,25} The inlet region consists of a wide area where the inlet hole ($0.7 \text{ mm in diameter}$) is punched (Fig. 1a). COMSOL simulations (Fig. S-2[†]) confirm that such an arrangement ensures an even distribution of cells among all the downstream channels. Each of these channels has a length of 5 cm, ensuring that particles have enough time to migrate to the center position prior to detection. This feature is clearly illustrated in Fig. 1d.¹⁹ The imaging region is located $\sim 48 \text{ mm}$ downstream of the inlet, where all component channels reunite into a common outlet (Fig. 1a). In addition, an array of microlenses is aligned to the center of the microchannels. This array has a width of $\sim 1330 \mu\text{m}$ and contains 11 microlenses (Fig. 1b) each with a spherical cap diameter (d) of $106 \mu\text{m}$ and height (h) of $39 \mu\text{m}$. It is important to note that im-

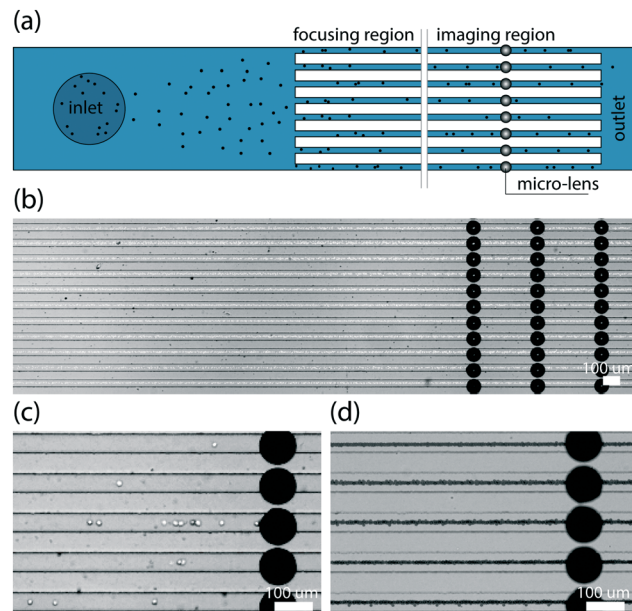


Fig. 1 (a) Schematic of the microfluidic device and detection scheme used in all experiments. (b) Image of eleven parallel microchannels (cross section of $53 \times 53 \mu\text{m}$). Microlenses are seen as dark, circular objects aligned on each channel (c) image of cells focused at the centerline of the channels passing underneath the lenses. (d) Image stack of PS beads passing under the micro lenses.

ages presented in Fig. 1 were recorded with the microscope objective focused onto the channels and not the lenses. Since the lenses create a virtual image of the beads several microns away from the microchannel (section 3.2; Microlens design), the beads cannot be observed underneath the lenses, which appear as black discs using this optical configuration (Fig. 1).

3.2 Microlens design

Spherical lenses were prepared *via* thermal reflow. Since surface quality plays an important role in defining the optical performance of a lens, surface profile and smoothness were assessed using a scanning electron microscope (SEM). A side view and a tilted side view of representative microlenses array are displayed in Fig. 2a. The average spherical cap diameter and height of the lenses were measured to be $106 \mu\text{m}$ and $39 \mu\text{m}$, respectively, and the gap between two microlenses approximately $15 \mu\text{m}$. The side view was generated by tilting the MLA, so as to incorporate more microlenses within the image. This explains why microlens shape appears to vary slightly in the bottom micrograph in Fig. 2a.

The optical properties of a lens are normally described by various parameters, including the back focal length (f_b), the numerical aperture (NA), magnification, and resolution. The lens diameter and central height of each lens determines each of these parameters (details provided in Fig. S-3[†]). Using a representative SEM image of a hemispherical lens (Fig. 2a), the radius of the curvature, R , can be determined according to the spherical cap approximation (eqn (1)) or measured directly as shown in Fig. S-4[†].

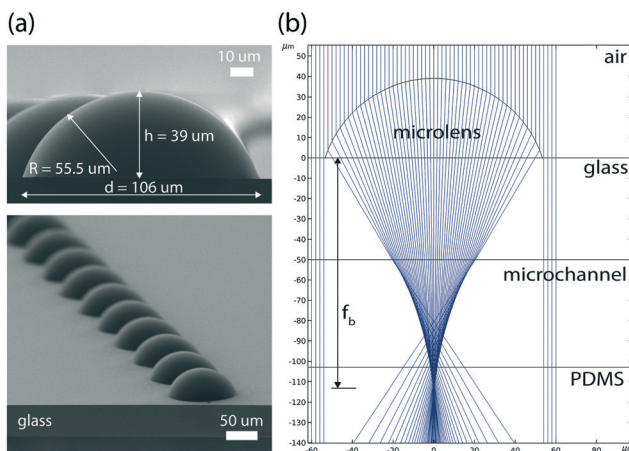


Fig. 2 (a) The SEM micrograph of the fabricated microlenses, (b) simulation showing the ray trajectories through the optofluidic device, simulated with a ray-tracing software package (COMSOL Multiphysics). The microlens ($n \sim 1.52$) sits on the $50 \mu\text{m}$ glass substrate ($n = 1.523$) seen in the bottom of panel a, followed by the $53 \mu\text{m}$ fluidic channel with the sample carrier fluid ($n = 1.3914$) and finally a PDMS layer ($n = 1.400$).

$$R = \frac{d^2 + 4h^2}{8h} \quad (1)$$

The back focal length, f_b , is defined as the distance between the focal plane of a collimated beam passing through the microlens and the glass substrate. Based on the characteristic parameters extracted from the profile curve, the focal length, numerical aperture and resolution of each lens can be calculated using the following expressions.²⁶

$$f_b = n_2 \frac{n_1 R - (n_1 - 1)h}{n_1(n_1 - 1)} \quad (2)$$

$$\text{NA} = n_2 \left\{ \left[\frac{2n_2}{n_1 D(n_1 - 1)} \right] R [Rn_1 - (n_1 - 1)h] + 1 \right\}^{-0.5} \quad (3)$$

$$\text{Resolution} = \frac{0.61\lambda}{\text{NA}} \quad (4)$$

Here, n_1 (the real part of the refractive index of the lens) is equal to 1.52 (see Fig. S-5 and Table S-1† for details of this measurement) and n_2 (the real part of the refractive index of glass) equal to 1.52. R and h are calculated through knowledge of the thickness of the photoresist layer and the diameter of the patterned cylinder, both determined from the SEM image shown in Fig. 2a. To ensure efficient imaging of mammalian cells (Jurkat and human B lymphocytes) flowing within the $53 \times 53 \mu\text{m}$ cross section channel, we manufactured microlenses having a spherical cap diameter of $106 \mu\text{m}$ and a height of $39 \mu\text{m}$. These dimensions yield a focal length of $123 \mu\text{m}$ and a NA of 0.64, as predicted by eqn (2) and (3) and the ray-tracing simulation (around $115 \mu\text{m}$) presented in Fig. 2b.

The fabrication of a lens suited to a specific application involves the consideration of a number of properties, such as f_b , FOV, magnification, resolution and numerical aperture. For example, Fig. 3 illustrates how f_b influences image formation, magnification and resolution. For imaging applications, it is important that $f_b \neq$ object distance (u). However, for signal enhancement the object should be at the focal length of the lens ($f_b = u$) as previously reported by Fan *et al.*⁶ In the situation depicted in Fig. 3a, image formation and thus magnification will depend upon the object distance, the image distance (v) and the focal length. It is well known that a real image (blue) is formed when $f_b < u < 2f_b$ and a virtual image (green) is formed when $u < f_b$. Moreover, magnification is related to the focal position according to following relationship:

$$\text{Magnification} = \frac{v}{u} = \frac{f_b}{u - f_b} \quad (5)$$

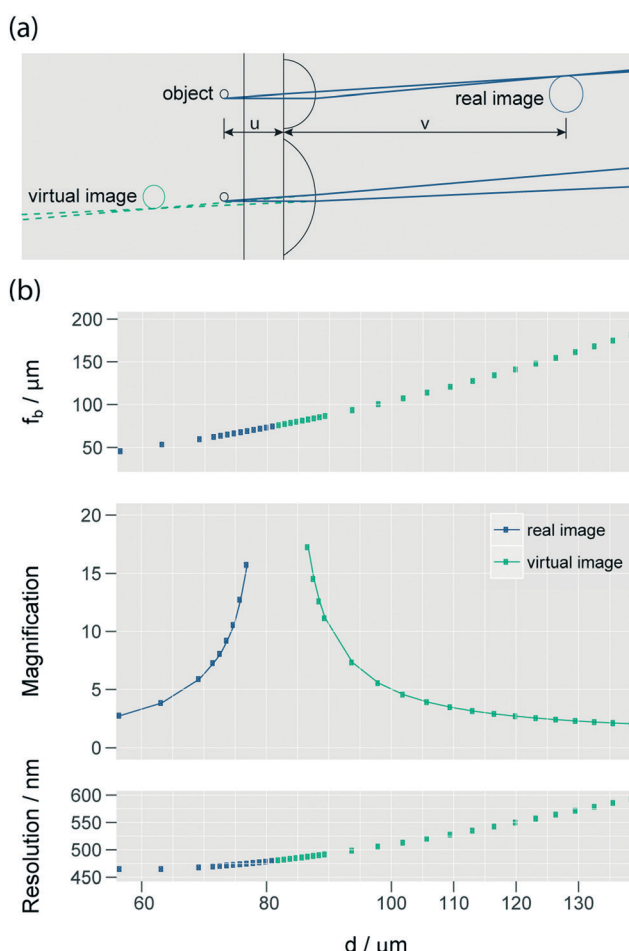


Fig. 3 (a) Ray tracing simulations, for two different lens dimensions: $h = 40 \mu\text{m}$ and $d = 63$ and $94 \mu\text{m}$, respectively. The object represents a $10 \mu\text{m}$ particle with an object distance, u , of $75 \mu\text{m}$. In the case where $f_b < u < 2f_b$ a real (blue) image is formed, and for $u < f_b$ a virtual (green) image is formed. (b) The dependence of resolution, magnification and focal length f_b on the lens diameter d for a constant lens height of $40 \mu\text{m}$.

Ray tracing simulations in COMSOL indicate that for a microlens with a focal length of 120 μm and an object distance of 76.5 μm , a magnified virtual image will be projected on the same side of the object, since the distance between the object and lens is less than the focal length. To better understand the dependence of f_b on lens geometry, the relationship between microlens diameter and the focal length (for a fixed height of 40 μm) is presented in Fig. 3b. Significantly, these data quantitatively validate our expectation that f_b varies quasi-linearly with lens size. For example, increasing the lens diameter from 60 μm to 130 μm , leads to an increase in the focal length (from 51 μm to 173 μm) and a reduction in numerical aperture from 0.72 to 0.58, as calculated from eqn (3).

Fig. 3 illustrates how magnification and resolution vary with diameter for a constant sphere cap height of 40 μm and an object distance of 75 μm . If f_b is in the range of u , magnification increases asymptotically towards infinity as a function of d , with a transition between a real and virtual image occurring when $u = f_b$ ($d = 81 \mu\text{m}$). In addition, and as predicted by raytracing simulations, resolution (Fig. 3b, bottom) is also a function of microlens size. For example, a micro-fabricated lens with a diameter (d) of 106 μm and height of 39 μm generates a magnification of approximately 4 \times and a resolution of 520 nm. Based on these predictions and the need to image mammalian cells (5–20 μm typical size) within the 53 \times 53 μm cross-section channel, we aimed to manufacture an array of microlenses having a diameter of 106 μm and a height of 39 μm .

Finally, it should be noted that, in theory, lenses of high numerical aperture tend to generate higher resolution images at the cost of a smaller FOV. Ray tracing simulations, shown in Fig. S-6,[†] indicate that fabricated lenses (with $d = 106 \mu\text{m}$ and $h = 39 \mu\text{m}$) have a FOV of 18 μm and a magnification of 3.6 \times . This value closely matches the experimental value of 3.2 \times , measured using 10 μm beads and a 2 \times objective lens (Fig. 4a). The small difference in magnification most likely originates from variations in the refractive index and thickness of the glass slide.

3.3 High-speed bright field imaging

Cellular images contain a variety of information that is often difficult to retrieve using low magnification imaging approaches. This includes information regarding morphological features or textures.¹⁶ To evaluate the capacity of the current microfluidic platform to operate as an imaging flow cytometer, a mixed population of polystyrene beads (with average diameters of 8 μm and 10 μm , and a standard deviation <0.2 μm) was injected into the microfluidic device, and focused *via* the aforementioned elasto-inertial approach. To obtain blur-free images of each bead (at average velocities of approximately 0.06 m s^{-1}), a high-speed CMOS camera was operated at up to 9000 frames per second, with an exposure time of 1 μs . Fig. 4a illustrates a representative image generated using only a 2 \times objective lens for a sample containing

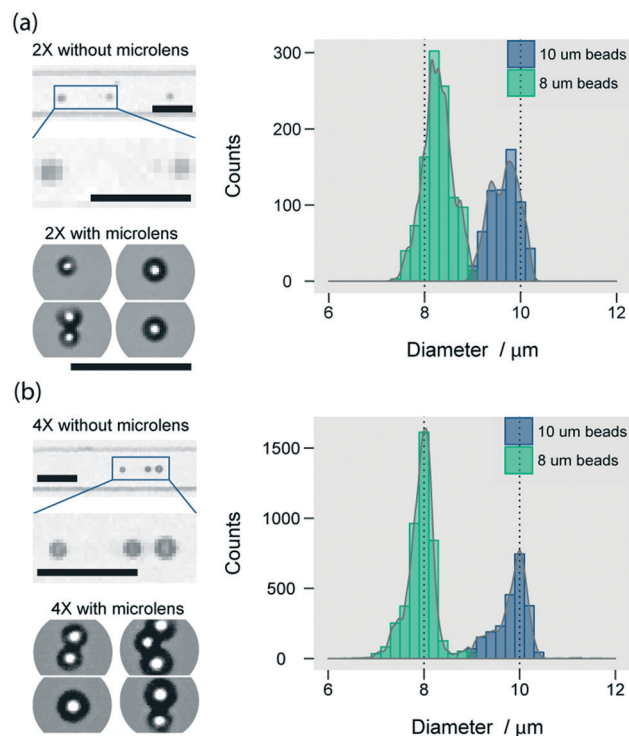


Fig. 4 Lens performance for the analysis of a mixture of beads with diameters of 8 μm and 10 μm (concentration: 4×10^6 particles per mL). (a) Beads are imaged with a 2 \times objective lens, without microlenses and in the presence of microlenses (providing an additional magnification of 3.2 \times). The histogram confirms efficient discrimination of two different bead populations in the presence of microlenses. (b) The mixture of beads is also imaged with a 4 \times objective without microlenses and in the presence of microlenses (providing an extra magnification of 3.2 \times). The images obtained with both the 4 \times objective and the micro lens offer higher resolution and more pixels per bead. They are therefore better suited for image processing algorithms than the 2 \times plus micro lens images. The scale bars are 50 μm .

8 μm and 10 μm diameter latex beads at a concentration of 4×10^6 beads per mL. It can be seen that size discrimination under these conditions is challenging since each bead is only represented by a few pixels. Images acquired in the presence of microlenses produced an additional magnification of 3.2 \times (Fig. 4a) and the different bead sizes can be distinguished from the distribution of sizes in the corresponding histogram of Fig. 4a. When using a 4 \times objective lens the microlenses achieve superior bead size discrimination, as can be clearly observed in Fig. 4b. In these images it is clear that bead aggregates can be magnified sufficiently to be resolvable when passing underneath the lens array.

The analysis of cells rather than beads is always more challenging due to reduced image contrast. A sample consisting of a suspension of Jurkat cells and human B lymphocytes cells at a concentration of $\sim 3 \times 10^6$ cells per mL was first imaged individually and then as a mixture (Fig. 5). The average cell flow velocity was approximately 0.05 m s^{-1} and the camera exposure time was set to 1 μs at a frame rate of 6000 frames per second. All other experimental parameters were the same as those used in the beadimaging experiments.

In the cell mixture a small population of 5 micron beads was also included and used as a “control” to measure the magnification of the lenses. Cell images obtained when using a $2\times$ objective lens appear quite blurry, but the presence of microlenses significantly enhances the imaging resolution (Fig. 5 left part). Images with even higher resolution can be obtained when using a $4\times$ objective lens in combination with the on-chip microlenses (Fig. 5a, right panel). In addition, the cells depicted in these images are transparent with sub-cellular features being clearly visible. As a result, accurate size information for Jurkat and hB cells can be extracted, with the resulting size distribution histograms confirming a broad distribution of cell diameters, ranging between 10 and 17 μm for Jurkat cells and between 6 and 12 μm for hB cells (Fig. 5b and c). When the mixture of the two cell lines was imaged in the presence of microlenses, the size distribution is significantly broader showing two subpopulations despite the inherent wide cell size distribution amongst these two populations. This size difference distribution of $2.4\ \mu\text{m}$ agrees very well with the FACS measurements (see Fig. S-7†). Throughput is very important when analyzing or screening a large volume of sample, but is rather challenging for conventional objective-lenses with an imaging field-of-view typically less than $2\ \text{mm}^2$. The mismatch between the active area of the microfluidic device and the FOV of the microscope-objective necessitates the capture of multiple images while scanning the sample. To address this important requirement for high-throughput imaging, we demonstrated that the on-chip lens detection platform can obtain high resolution images of cells or micron-sized beads over an ultra-wide FOV.

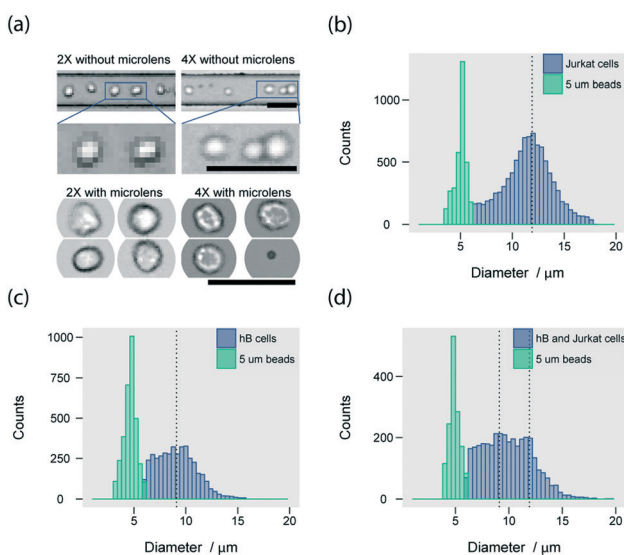


Fig. 5 (a) Jurkat cells imaged with $2\times$ and $4\times$ objectives and with an additional $3.2\times$ from the microlens array. (b) Histogram of the extracted size distribution of a population of Jurkat cells. The sample was spiked with 5 μm PS beads to reference for size. The average diameter is approximately 12 μm . (c) Size distribution of hB cells spiked with 5 μm beads. (d) A mixed population of hB and Jurkat cells yields a broader distribution, however the average diameters of the two individual cell types are still discernible. The scale bars are 50 μm .

The use of low magnification objectives offers the advantage of an increased field of view that can encompass many parallel microfluidic channels, as shown in Fig. 6. More specifically, when imaging with a $2\times$ objective, the FOV of our sensor camera can cover 68 microlenses that can be aligned in the middle of all 68 parallel channels (Fig. 6b and c). Here, it should be noted that these microlenses provided a magnification of $\sim 2.4\times$ since they possess a different geometry ($d = 63\ \mu\text{m}$, $h = 30\ \mu\text{m}$) than the ones used in the previous experiments (Fig. 4 and 5). When fabricating large arrays, smaller lens dimensions were chosen, due to the ease of fabrication and a larger inter-lens gap between. Furthermore, we wanted to exploit the difference between a lens with a virtual and real image, as presented in Fig. 3b. A smaller lens of fixed magnification will generate a darker image with less contrast due to more pronounced spherical aberration, although the theoretical resolution will be higher. The use of 1000 ppm 0.4 MDa PEO allows focusing of 10 μm beads at flow velocities of $0.12\ \text{m s}^{-1}$, as shown in Fig. 6a. At this velocity, particles need only 0.24 ms to cross the FOV of a micro lens ($\approx 29\ \mu\text{m}$), hence theoretically a minimum frame rate of 4137 fps is required for accurate sampling. However, because cells or beads can only be properly imaged if they are centered to the microlens, we choose a higher frame rate for the experiment (10 000 fps). A higher frame rate results in oversampling with respect to the number of beads acquired. On the other hand, $\sim 50\%$ of the images containing beads depicted only partially, are discarded in the image processing. After background subtraction, an image-processing algorithm written in Python

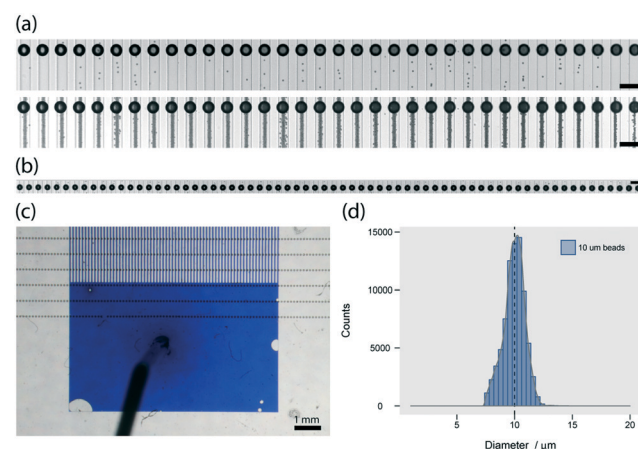


Fig. 6 (a) Images of 34 channels along with 34 aligned micro lenses imaged with a $4\times$ objective. The top image shows a snapshot of individual 10 μm PS particles, with the bottom depicting an image-stack of 500 images (b) image representing 68 microchannels equipped with micro lenses. (c) The entire imaging platform consists of 68 microchannels. The outlet part, channels and tubing are filled with blue ink. The black lines mark the micro lenses, for simpler alignment there are multiple rows. Lenses have a dimensions of $h = 30\ \mu\text{m}$, $d = 63\ \mu\text{m}$, and a measured magnification of $2.4\times$, which agrees well with simulations (Fig. 3b). (d) Histogram showing the diameter of 10 μm beads measured with a $4\times$ objective in 34 channels and at a throughput around 50 000 beads per second. Scale bars are 100 μm if not labeled differently.

was used to find the contours of the beads, as shown in Fig. S-1 and Note S-1.[†] Using a 4 \times objective, 34 lenses (Fig. 6a) can be placed in the region of interest, yielding a throughput of 50 000 events per second and excellent size determination as shown in Fig. 6d. Eventually, using a 2 \times objective, 68 lenses can be used (Fig. 6b), potentially yielding a throughput of up to 100 000 events per second. Accordingly, the proposed imaging flow cytometer, through the use of on-chip lenses, can combine the high throughput of a multiplexed system with the imaging resolution of high magnification optics.

4. Conclusion

In summary, we have successfully developed integrated refractive microlens arrays fabricated by a thermal reflow process and investigated their optical properties based on their geometry. Such knowledge enables precise design of an array of microlenses for specific application, such as imaging flow cytometry in the current work. The effectiveness of the arrays in imaging flow cytometry was investigated via both simulations and experimental studies. Furthermore, the use of elasto-inertial focusing as a sheathless approach to focusing cells in a single file within a series of parallel microfluidic channels enables the use of high flow velocities, ensures utilization of the entire CMOS sensor and thus maximizes the number of cells detected per acquisition frame. The microfluidic-based microlens array not only provides for optical performance equivalent to that of a high magnification microscope objective, but it also enhances the throughput in wide field imaging and enumeration of cells; a key benefit in applications such as rare cell analysis. Notably, the integration of microlenses with microfluidic devices will undoubtedly catalyze new applications such as light focusing,²⁷ *in situ* monitoring, optical imaging in flow cytometry,^{28,29} as well as the efficient monitoring of protein/DNA micro-arrays.

Conflicts of interest

There are no conflicts to declare.

Acknowledgements

This work was partially supported by the Swiss Federal Institute of Technology (ETH Zürich) and the National Research Foundation of Korea (Grant Nos. 2008-0061891 and 2009-00426).

References

- 1 A. S. Stender, K. Marchuk, C. Liu, S. Sander, M. W. Meyer, E. A. Smith, B. Neupane, G. Wang, J. Li and J.-X. Cheng, *et al.*, *Chem. Rev.*, 2013, 113, 2469–2527.
- 2 A. Tripathi, T. V. Chokshi and N. Chronis, *Opt. Express*, 2009, 17, 19908–19918.
- 3 A. Tripathi and N. Chronis, *J. Micromech. Microeng.*, 2011, 21, 105024.
- 4 D. Wu, L.-G. Niu, S.-Z. Wu, J. Xu, K. Midorikawa and K. Sugioka, *Lab Chip*, 2015, 15, 1515–1523.
- 5 L. Chang, M. Dijkstra, N. Ismail, M. Pollnau, R. M. de Ridder, K. Wörhoff, V. Subramaniam and J. S. Kanger, *Opt. Express*, 2015, 23, 22414–22423.
- 6 Y. Fan, Y. Wu, Y. Chen, Y. C. Kung, T. Wu, K. Huang, H. J. Sheen and P. Y. Chiou, *Biomicrofluidics*, 2013, 7, 044121.
- 7 M. N. Gulari, A. Tripathi, M. Ghannad-Rezaie and N. Chronis, *Micromachines*, 2014, 5, 607–621.
- 8 S. Biehl, R. Danzebrink, P. Oliveira and M. A. Aegeirter, *J. Sol-Gel Sci. Technol.*, 1998, 13, 177–182.
- 9 N. Ong, Y. Koh and Y. Q. Fu, *Microelectron. Eng.*, 2002, 60, 365–379.
- 10 S.-d. Moon, S. Kang and J.-U. Bu, *Opt. Eng.*, 2002, 41, 2267–2270.
- 11 J. Albero, L. Nieradko, C. Gorecki, H. Ottevaere, V. Gomez, H. Thienpont, J. Pietarinen, B. Päiväranta and N. Passilly, *Opt. Express*, 2009, 17, 6283–6292.
- 12 F. T. O'Neill and J. T. Sheridan, *Optik*, 2002, 113, 391–404.
- 13 S. Kim, M. Choi, H. Kim, J. Lim and S. Kang, *Electron. Lett.*, 2008, 44, 492–493.
- 14 J. Lim, P. Gruner, M. Konrad and J.-C. Baret, *Lab Chip*, 2013, 13, 1472–1475.
- 15 E. Schonbrun, A. R. Abate, P. E. Steinurzel, D. A. Weitz and K. B. Crozier, *Lab Chip*, 2010, 10, 852–856.
- 16 E. Schonbrun, S. S. Gorthi and D. Schaak, *Lab Chip*, 2012, 12, 268–273.
- 17 S. K. Sia and L. J. Krucka, *Lab Chip*, 2008, 8, 1982–1983.
- 18 D. Di Carlo, D. Irimia, R. G. Tompkins and M. Toner, *Proc. Natl. Acad. Sci. U. S. A.*, 2007, 104, 18892–18897.
- 19 G. Holzner, S. Stavrakis and A. deMello, *Anal. Chem.*, 2017, 89, 11653–11663.
- 20 A. Leshansky, A. Bransky, N. Korin and U. Dinnar, *Phys. Rev. Lett.*, 2007, 98, 234501.
- 21 G. Romeo, G. D'Avino, F. Greco, P. A. Netti and P. L. Maffettone, *Lab Chip*, 2013, 13, 2802–2807.
- 22 P. Nussbaum, R. Voelkel, H. P. Herzig, M. Eisner and S. Haselbeck, *J. Opt.*, 1997, 6, 617.
- 23 A. Schilling, R. Merz, C. Ossmann and H.-P. Herzig, *Opt. Eng.*, 2000, 39, 2171–2176.
- 24 C. A. Schneider, W. S. Rasband and K. W. Eliceiri, *Nat. Methods*, 2012, 9, 671.
- 25 D. Yuan, S. H. Tan, Q. Zhao, S. Yan, R. Sluyter, N.-T. Nguyen, J. Zhang and W. Li, *RSC Adv.*, 2017, 7, 3461–3469.
- 26 J. Chen, W. Wang, J. Fang and K. Varahramyan, *J. Micromech. Microeng.*, 2004, 14, 675.
- 27 L. Dong, A. K. Agarwal, D. J. Beebe and H. Jiang, *Nature*, 2006, 442, 551–554.
- 28 P. Fei, Z. He, C. Zheng, T. Chen, Y. Men and Y. Huang, *Lab Chip*, 2011, 11, 2835–2841.
- 29 A. S. Rane, J. Rutkauskaitė and S. Stavrakis, *et al.*, *Chem.*, 2017, 3, 588–602.